Liu *et al. Biochar* (2023) 5:74
https://doi.org/10.1007/s42773-023-00276-0

Biochar

ORIGINAL RESEARCH

Open Access

Ice-phobic properties of MoS_2-loaded rice straw biogas residue biochar-based photothermal and anti-corrosion coating with low oxygen to carbon ratio

Zhiyuan Liu[1], Yan Li[1,3*] and Zhiyuan He[2*]

Abstract

Icing of wind turbine blades will seriously hinder the development of the wind power industry, and the use of biomass resources to solve the icing problem is conducive to promoting the synergistic development of biomass and wind energy. In this study, ice-phobic coatings with photothermal and anti-corrosion properties were prepared by surface modification pyrolysis and hydrothermal reaction with rice straw biogas residue as raw material. The erosion of KOH and the surface modification of MoS_2 produced a rough structure of the material, and the high-temperature pyrolysis and hydrothermal reaction promoted the dehydrogenation and decarboxylation reactions, which reduced the number of oxygen-containing functional groups and decreased the surface energy of the material. The ice-phobic coating has superhydrophobic properties with a contact angle of 158.32°. Due to the small surface area in contact with water, the coating was able to significantly reduce the icing adhesion strength to 53.23 kPa. The icing wind tunnel test results showed that the icing area and mass were reduced by 10.54% and 30.08%, respectively, when the wind speed was 10 m s^{-1} and the temperature was − 10 ℃. Photothermal performance tests showed that the MoS_2-loaded material had light absorption properties, and the coating could rapidly warm up to 58.3 ℃ under xenon lamp irradiation with photothermal cycle stability. The loading of MoS_2 acts as a physical barrier, reducing the contact of corrosive media with the substrate, thus improving the anti-corrosion of the coating. This study has practical application value and significance for the development of the anti-icing field under complex environmental conditions.

Highlights

1. A biochar-based ice-phobic coating was prepared from rice straw biogas residue.
2. Low O/C ratio promoted superhydrophobicity and low ice adhesion of the coating.
3. The icing wind tunnel test proved the coating has good anti-icing performance.
4. The MoS_2 loading endowed the material with photothermal and anti-corrosion effects.

Handling Editor: Xiangzhou Yuan.

*Correspondence:
Yan Li
liyanneau@neau.edu.cn
Zhiyuan He
hezy@bit.edu.cn
Full list of author information is available at the end of the article

Keywords Wind turbine blades, Ice-phobic coating, Rice straw biogas residue biochar, Icing wind tunnel tests

Graphical Abstract

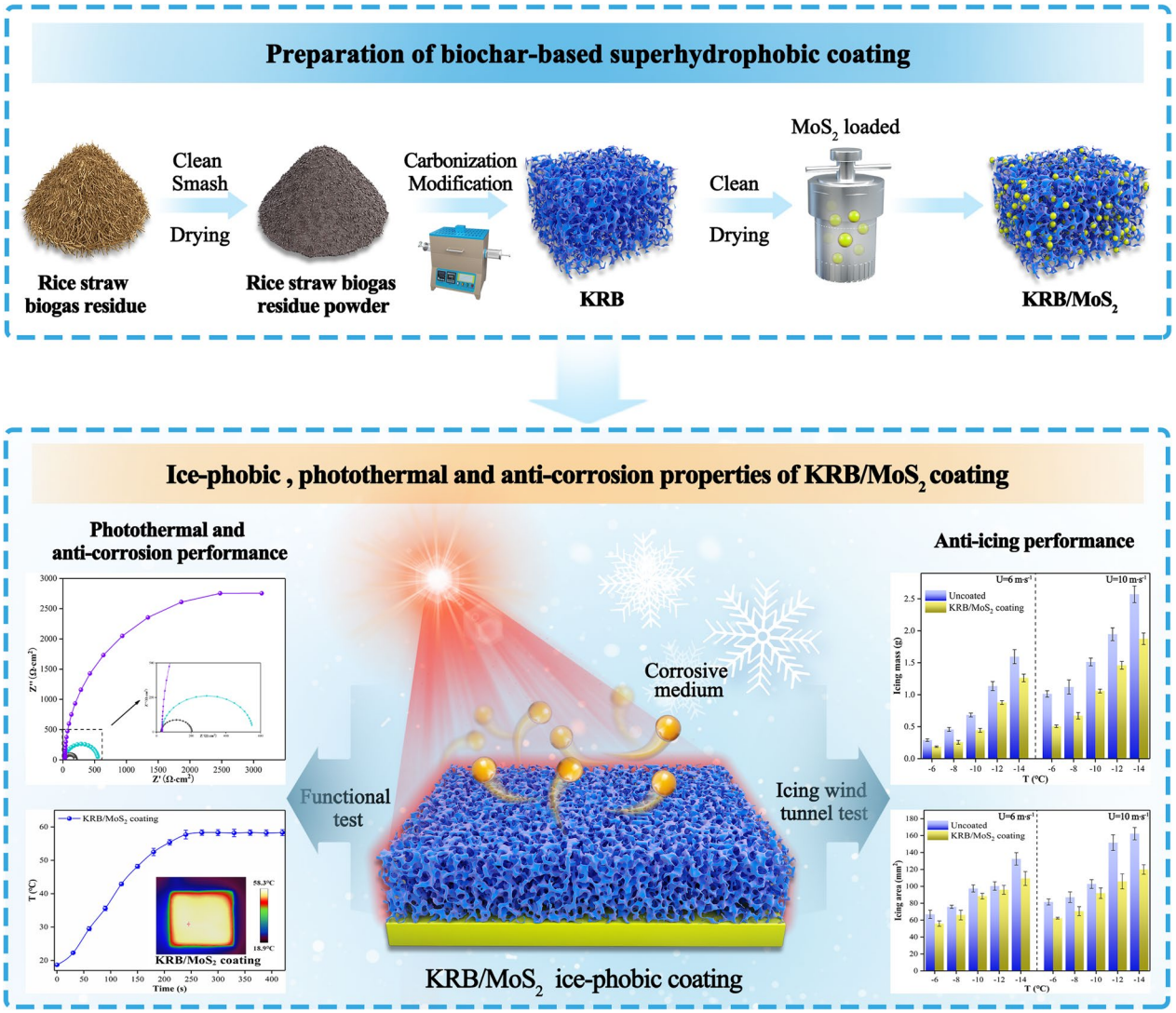

1 Introduction

The current shortage of traditional fossil energy sources and the increasing environmental pollution and greenhouse effect have led to widespread interest in renewable and clean energy sources (Hui et al. 2022; Xu et al. 2022). Among the many alternative energy options, wind energy and biomass energy have seen rapid development due to abundant reserves and non-pollution (Ju et al. 2023b; Kumar et al. 2023). Biomass can be used to obtain energy through direct combustion, anaerobic digestion or gasification of biomass, and porous carbon materials rich in carbon and with high specific surface area can also be obtained by pyrolysis (Liu et al. 2020; Xu et al. 2023). The raw materials used in the preparation of biochar are usually agricultural wastes, which effectively ensures the resourceful use of these wastes (Liu et al. 2022). Biochar has the potential to store carbon over the long term, reduce greenhouse gas emissions, and can also immobilize hazardous substances in biochar to reduce the risk of pollution to the environment (Wang et al. 2023c). Wind power generation is a main way to participate in the development and

utilization of new energy (Li et al. 2023; Tong et al. 2023). The geographical environment and climatic conditions of wind power plants cause the icing of wind turbine blades, endangering the efficient operation of wind turbines and resulting in reduced operational efficiency (Guo et al. 2021; Zhang et al. 2023b). Therefore, solving the blade icing problem through efficient anti-icing and de-icing technology is crucial to ensure the safe operation of the power system (Zheng et al. 2023). At present, anti-icing technology mainly includes mechanical de-icing, solution de-icing and thermal de-icing, but there are shortcomings such as high manual work intensity, short de-icing duration and high energy consumption (Cheng et al. 2023; Liu et al. 2023a; Yue et al. 2023). The development of a safe and reliable blade anti-icing technology is of great significance for improving the power generation efficiency of wind turbines and extending the service life of wind turbines (Xue et al. 2023b).

Anti-icing materials can prevent or retard the formation of ice on the surface of objects and are of great value in mitigating the adverse effects of natural icing (Huang et al. 2022; Ju et al. 2023a; Wu et al. 2022). Therefore, the selected anti-icing material should have a low solid-liquid contact area, which can effectively reduce the heat exchange rate to achieve the anti-icing effect (Shamshiri et al. 2023; Yang et al. 2022). The superhydrophobic surface can retain air and decrease heat transfer due to its micro-nano structure, delay ice nucleation and reduce ice accumulation in the condensation stage, thus effectively delaying the freezing time (Xiang et al. 2023). Photothermal materials have high photothermal conversion efficiency and no chemical pollution, with the advantages of energy savings and environmental protection in the field of anti-icing materials gradually attracting attention (Guo et al. 2020; Xue et al. 2023a). Solar energy, a promising clean and renewable energy source, holds the potential to satisfy human energy needs and reduce reliance on fossil fuels (Hou et al. 2023; Molnár et al. 2022). The utilization of the photothermal effect exhibited by photothermal materials represents a novel approach to retarding ice formation or directly melting ice (Wu et al. 2021). The combination of photothermal active de-icing and superhydrophobic passive anti-icing is expected to improve the de-icing efficiency of the coating. However, the existing coating is susceptible to mechanical damage and chemical corrosion under the influence of extreme weather, resulting in the loss of anti-icing performance (Zhang et al. 2022). By introducing nanoparticles into the coating, the researchers can not only provide micro-nano structures to enhance hydrophobicity but also improve wear and corrosion resistance, offering new ideas for the structural control and construction of anti-icing materials.

The selection of raw materials for the ice-phobic coating is based on a combination of inexpensive, superhydrophobic and other application requirements, and polymeric organic materials rich in hydrocarbons and other low surface energy groups can be chosen (Guan et al. 2023; Ke et al. 2022; Miao et al. 2023). Biomass raw materials are usually renewable resources, and compared with traditional chemical raw materials, the ice-phobic coating prepared from biomass has lower carbon emissions and environmental impact (Kumar et al. 2023; Liu et al. 2023c). Lignin, cellulose and hemicellulose in biomass raw materials are mainly composed of carbon skeletons connected by carbon–hydrogen bonds, which can be chemically modified using appropriate methods to obtain compounds with hydrophobicity so that ice is not easily adhered to the coating surface (Wang et al. 2023b). The carbonized biomass raw materials form a rough structure, which not only helps to improve the fluidity of liquid and prevent the formation and accumulation of ice, but also reduces the contact area between the coating surface and ice, thus enhancing the anti-icing effect (Liu et al. 2023b). In addition, the composite of biochar with different particles exhibits special functionalities of the material, thus increasing the anti-icing potential of the material. MoS_2 has a graphite-like layered structure with high absorption of visible and near-infrared light (Liu et al. 2021). Due to its layered structure and band-gap structure, it can absorb light in a wide wavelength range, and also has a fast photothermal response, which can convert the absorbed light energy into heat energy in a short period of time (Jlidi et al. 2021; Wang et al. 2023a). Moreover, the high chemical stability of MoS_2 makes it stable in air and different humidity environments, which makes MoS_2 have advantages in the anti-icing application of wind turbine blades. Using the properties of biochar and MoS_2, the preparation of a carbon-based ice-phobic coating by loading particles can promote the high-value utilization of biomass resources and assist in the safe development of wind power industry.

In this study, a superhydrophobic ice-phobic coating with photothermal and anti-corrosion properties was prepared from rice straw biogas residue after anaerobic digestion. The removal of hydrophilic groups and the loading of MoS_2 in biochar were achieved by pyrolysis and hydrothermal methods, which improved the hydrophobic properties of the material. The anti-icing performance of the coating under low-temperature conditions was investigated using icing wind tunnel tests. The anti-icing performance of the coating at low temperatures was studied using icing wind tunnel tests, which showed that its excellent superhydrophobicity slowed down the heat transfer rate and accelerated the roll-off of water droplets on the coating surface. Meanwhile, the internal rough

structure of the biochar-based coating enhanced the absorption of light, contributing to the increase in blade surface temperature in cold conditions and promoting the melting of ice. The loading of MoS_2 reduced the contact between the corrosive medium and the substrate, solving the problem of wind turbine blade corrosion. The research realized the clean utilization of biomass resources and had good prospects for application in blade anti-icing in cold regions.

2 Experimental section

2.1 Materials and chemical reagents

Potassium hydroxide (90%, KOH) was purchased from Macklin Biochemical Co., Ltd. Ethanol absolute (99.7%) was provided by Sinopharm Chemical Reagent Co., Ltd. Thioacetamide (99%) was bought from Tianjin Guangfu Pine Chemical Research Institute. Urea (99%) was bought from Tianjin Tianli Chemical Reagent Co., Ltd. Commercial-grade polyvinylidene difluoride (PVDF) was bought from Harbin Lithium battery factory in China. *N*-methyl pyrrolidone (99.5%, NMP) was purchased from Tianjin Zhiyuan Chemical Reagent Co., Ltd. All the chemicals were used without any further treatment.

2.2 Preparation of superhydrophobic ice-phobic coating

2.2.1 Preparation of modified rice straw biogas residue biochar

The rice straw biogas residue was washed with deionized water and then dried in an oven, after which it was crushed and sieved to obtain the rice straw biogas residue powder. Subsequently, the biogas powder was carbonized in a tube furnace (OTF-1200X, HF-kejing Material Technology Co., Ltd.) under a nitrogen atmosphere from room temperature to the target temperature at a rate of 5 ℃ min^{-1} with a platform temperature of 500 ℃ and held for 3 h. The biochar sample was collected after the tube furnace had cooled to room temperature and noted as biogas residue biochar (RB).

The prepared RB was mixed with activator KOH in a mass ratio of 2:1 and then placed in a tube furnace. The sample was heated to 800 ℃ at a heating rate of 10 ℃ min^{-1} and kept in a nitrogen atmosphere for 2 h, and then cooled to room temperature. The biochar was washed with 1 mol L^{-1} HCl, then washed with anhydrous ethanol and deionized water several times until it was neutral, and then dried, thus obtaining the KOH-modified biogas residue biochar (KRB).

In this study, biochar was prepared by carbonization and KOH modification. The carbonization process could remove volatile organic compounds, moisture and other impurities from biomass to obtain biochar with high thermal stability and carbon content. Because the premise of constructing hydrophobic materials was a certain rough structure, KOH modification could promote the formation of microporous and mesoporous structures and improve the roughness of materials.

2.2.2 Preparation of modified biogas residue biochar/MoS_2

The MoS_2-loaded biochar was prepared by a one-step hydrothermal method. 10 mg of biochar was dispersed in 15 mL of deionized water, and the biochar was fully dispersed by sonicate for 0.5 h. Then, 25 mL of ethanol, 30 mg of MoO_3, 35 mg of ammonium thioacetate and 300 mg of urea were added to the above solution respectively and stirred vigorously for 1 h to make the solution evenly dispersed. The obtained suspension was transferred to a 50 mL reaction kettle and reacted at 200 ℃ for 24 h. After the reaction kettle had cooled naturally to room temperature, the samples were removed, washed by centrifugation several times with deionized water and ethanol and finally dried in a vacuum drying oven at 40 ℃ for 12 h to obtain KOH-modified biogas residue biochar/MoS_2 (KRB/MoS_2).

The hydrothermal method was used to prepare KRB/MoS_2 materials because some oxygen atoms could be separated from the biochar in a high-temperature and high-pressure water environment, thus reducing or removing oxygen-containing functional groups and improving the hydrophobicity of the materials.

2.2.3 Coating of preparation

0.7 g of PVDF powder and 9.3 g of NMP were mixed in a 25 mL beaker and stirred until the PVDF was completely dissolved, and 7% PVDF was prepared as an adhesive for the coating, which was sealed for subsequent use. Then, 0.4 g of 7% PVDF solution was mixed with 0.2 g of biochar-based material in a 15 mL beaker, ultrasonically treated for 0.5 h, and stirred evenly. The sample was applied by scraping onto the plate and blade for subsequent testing. The coating was based on glass fiber reinforced plastic (FRP) commonly used in wind turbine blades. In the experiment, the size of flat substrate was 3 cm square, and the blades were NACA0018 airfoil with a chord length of 100 mm. To avoid experimental errors, the ice-phobic coating was sprayed onto three flat substrates and blades for the tests.

2.3 Characterizations of prepared materials

The sample was adhered to the sample stage using conductive adhesive and placed in a vacuum chamber for surface gold spraying. The treated sample stage was fed through the vacuum chamber into a scanning electron microscope (SEM, SU8010, Hitachi) for scanning and

observation. The specific surface area and pore size of the samples were analyzed by a specific surface area analyzer (ASAP2020, Micromeritics) after vacuum degassing at 100 ℃ for 2 h. The specific surface area of the sample was calculated by the Brunner-Emmet-Teller (BET) method, and the pore volume and pore diameter were obtained by the BJH method. Raman spectroscopy (LabRAM HR800) enabled the study of the defects and graphitization degree of biochar. The structure and functional groups of the samples were analyzed by a fourier infrared spectrometer (FTIR, Nicolet is50, Thermo Fisher), and the scanning wave number ranged from 500 to 4000 cm^{-1}. X-ray photoelectron spectroscopy (XPS, ESCALAB 250Xi, Thermo Fisher) was used to analyze the elemental composition, chemical valence state, and molecular formula composition of samples. The contact angle (CA) and sliding angle (SA) were measured by the CA meter (JCD2000D3M, Shanghai Zhongchen Digital Technic Apparatus CO., Ltd.) to characterize the wettability of the material surface. The static CA was measured by placing a 5 μL deionized water drop on the sample through a micro sampler, and the SA was measured by changing the tilt angle of the sample stage using an automatic suspension table. After filling a cube ice cube mold with a side length of 2.5 cm with water, the mold was covered with a square flat plate with a side length of 3 cm coated with different materials, and then was placed in a refrigerator with a temperature of − 20 ℃ for 12 h. The dynamometer was placed on the sample surface, and the frozen ice was pushed horizontally. The maximum shear force used to push the ice during the test was recorded, and the icing adhesion strength was calculated by Eq. (1) (Qi et al. 2023):

$$\tau = F/A \tag{1}$$

where τ is the ice adhesion strength (kPa); F is the tested ice adhesion force (N); A is the contact area between the ice and the material.

2.4 Icing wind tunnel test

The icing wind tunnel system was used to simulate the actual environment to investigate the anti-icing performance of the biochar-based coating. The blades were installed into the test section of the wind tunnel system before the icing test began, and the spray system was connected after the blades had been cooled to the test temperature (Mu et al. 2023). The experimental water was pressurized to form a uniform water mist and sprayed out, which was cooled to a supercooled state before coming into contact with the blades and freezing. Throughout the experiment, a camera captured the icing process for subsequent observation. Following the experiment, the blade was detached from the test section of the wind tunnel system, and the icing mass was measured using a balance.

2.5 Photothermal performance

UV-Vis-NIR absorption spectrum was generated through the transition of valence electrons, and it analyzed the absorption characteristics of light by molecules or ions of substances. UV-Vis-NIR spectrophotometer (UV-3600 Plus, Shimadzu) was employed to determine the optical absorbance of the samples in the spectral range of 200–2500 nm.

To test the photothermal properties of the material, the test sample was placed under a xenon lamp light source (BBZM-I), and the temperature change was monitored in real-time using a thermometer and a thermal infrared camera (H21 pro, Hikmicro) to take thermal infrared photographs of the sample. When the system temperature dropped to room temperature, the light source was turned on again to repeat the experiment, and the photothermal stability of the coating was explored by repeating the above process.

2.6 Anti-corrosion performance

The anti-corrosion performance of the coating was tested by an electrochemical workstation, and electrochemical impedance spectroscopy (EIS) was obtained. A three-electrode test system was used in the test, in which the working electrode, the counter electrode and the reference electrode were all 1 cm^2 coating samples, platinum electrodes and saturated calomel electrodes. EIS was measured by the controlled potential method, and the frequency range was 10^{-2}–10^5 Hz. The corrosion medium was 3.5 wt% NaCl solution.

2.7 Wear resistance test

To qualitatively assess the mechanical stability and resistance of the coating, sandpaper friction tests were conducted. The coating was placed on the surface of sandpaper (800 grit) and a 100 g weight was placed on the top of the sample. The sample was pulled to advance 10 cm on the surface of the sandpaper in one cycle and after each cycle the sample was removed and the CA was measured.

3 Results and discussion

3.1 Characterization analysis

SEM analysis was carried out to gain a comprehensive understanding of the morphology of the biochar material. The surface of the RB was relatively smooth, with a degree of folded structure present (Fig. 1a). As can be seen from Fig. 1b, the etching of the material by KOH resulted in a rougher KRB surface and the formation of

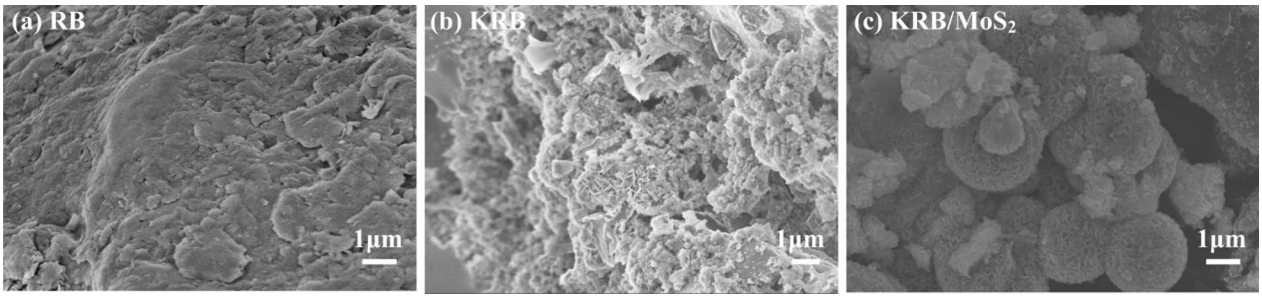

Fig. 1 SEM images of **a** RB, **b** KRB and **c** KRB/MoS_2

an irregularly shaped porous structure in the presence of the activator. The increased surface roughness of materials provided the basis for the construction of superhydrophobic materials. The MoS_2-loaded biochar surface had a large number of lamellar structures (Fig. 1c), which proved the successful preparation of KRB/MoS_2 and offered barrier properties to corrosive media entering the substrate surface. The element mapping (Additional file 1: Fig. S1a) indicated three elements dispersed on the KRB/MoS_2 surface, with C being the dominant element of the biochar, and the elements Mo and S originating from the MoS2 and being uniformly distributed over the biochar. The High-Resolution Transmission Electron Microscopy (HRTEM) characterization showed that the biochar composite composed of KRB and MoS_2 had been successfully synthesized. It could be seen from Additional file 1: Fig. S1b, c that MoS_2 grew on the biochar surface and had an obvious layered structure.

To further investigate the specific surface area and pore size of biochar, nitrogen adsorption and desorption tests were conducted on the samples. When the relative pressure was less than 0.3, between 0.3 and 0.9, and between 0.9 and 1, it was related to the micropores, mesopores and macropores of the material, respectively. In Fig. 2a, the adsorption–desorption curve of RB showed a typical type III adsorption type, indicating that the material was macro-porous or non-porous (Yoon et al. 2017). The adsorption and desorption curves of KRB and KRB/MoS_2 showed typical type I adsorption, indicating that the material had a large specific surface area and pore volume, a small average pore size and a high proportion of micropores (Zhang et al. 2023a). Figure 2b shows the pore size distribution of the different materials, and it could be seen that the pore volumes of RB tended to be close to 0, while the pore volume of KRB and KRB/MoS_2 increased greatly after KOH modification. And the pore sizes were concentrated in the <4 nm range, indicating that KOH promoted the pore generation of biochar materials. From Table 1, the specific surface area and pore volume of unmodified biochar were positively small, while the specific surface area and pore volume of KRB increased dramatically to 1492.69 $m^2\ g^{-1}$ and 1.08 $cm^3\ g^{-1}$, with 37.04% of micropores. Although there was a decrease in the specific surface area and pore volume of KRB/MoS_2, and the formation of MoS_2 increased the average pore size to 3.33 nm, the lamellar structure formed by the MoS_2 loading was able to increase the material roughness, further contributing to the formation of the rough pore structure required for superhydrophobic materials.

As shown in Fig. 2c, the two characteristic peaks of the Raman spectrum were located at 1349 cm^{-1} and 1588 cm^{-1} respectively, which could be attributed to the D peak and G peak of the carbon material . The D peak was related to the sp^3 structure and indicated the amorphous structure and defects of the carbon material, while the G peak was a characteristic peak of the sp^2 structure and reflected the symmetry and crystallinity of the carbon. The intensity ratio (I_D/I_G) of D peak and G peak could reflect the ratio of disorder degree to ordered graphitized carbon, that was, the graphitization degree of the carbon material. The I_D/I_G values for RB and KRB were 0.88 and 0.96, respectively, with the increase in the ratio primarily arising from the augmented defects on the surface of KRB. Moreover, the I_D/I_G ratio for KRB/MoS_2 was 0.99, resulting from the intensified disorder and further reduction in the degree of graphitization due to the MoS_2 loading.

The chemical structures and functional groups of RB, KRB and KRB/MoS_2 were analyzed by FTIR. It was clear from Fig. 2d that the surface functional groups changed significantly after the surface modification. A broad absorption peak near 3460 cm^{-1} was attributed to the O–H bond stretching vibration absorption peak. The absorption peak around 2930 cm^{-1} belonged to the stretching vibration peak of the $-CH_3$ group and the low surface energy of C–H could promote the hydrophobic property of the material (Karkoosh et al. 2023). The stretching vibrational peaks of MoS_2 were at 1600 cm^{-1}, 1470 cm^{-1} and 980 cm^{-1}, respectively

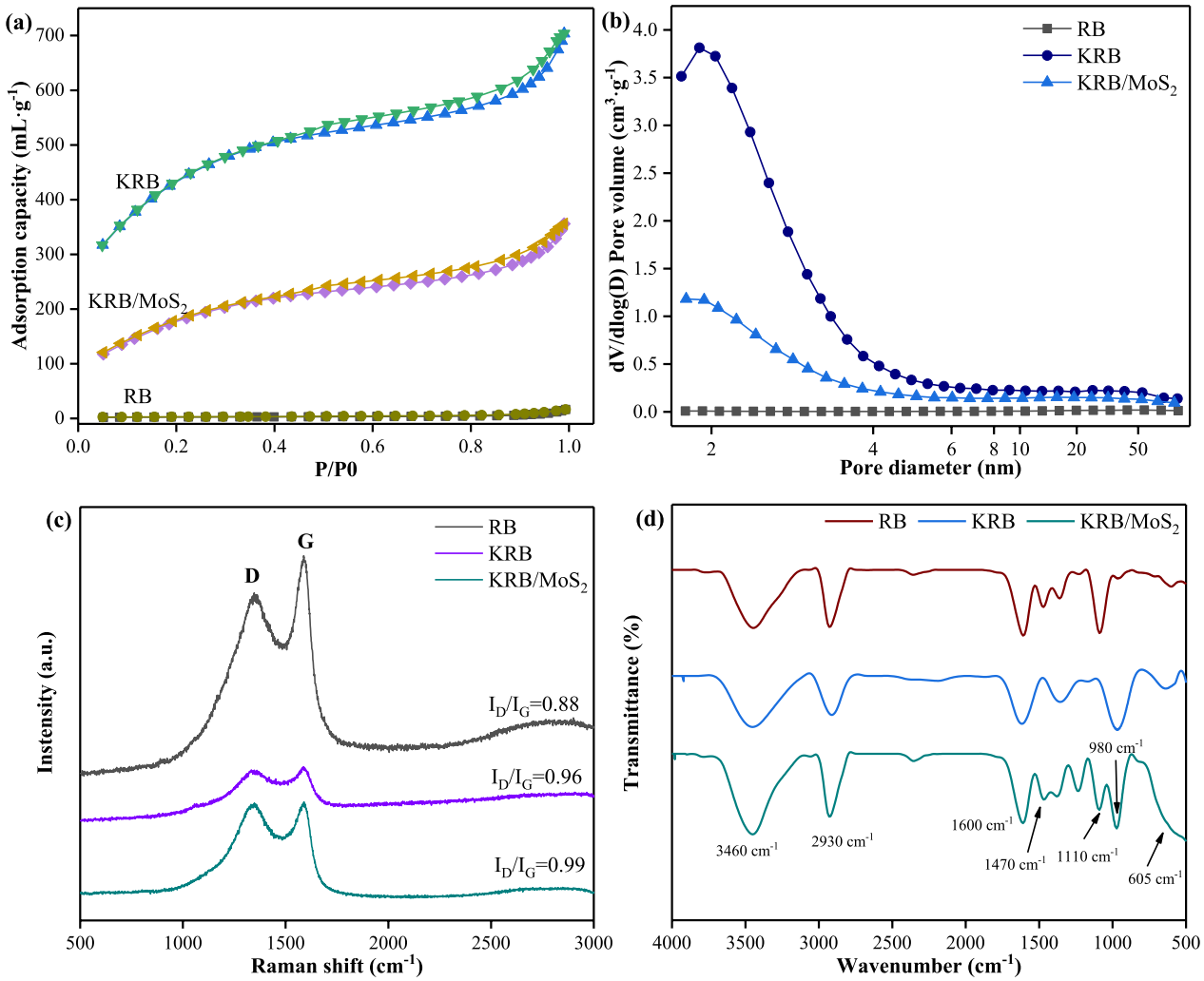

Fig. 2 **a** Nitrogen adsorption–desorption isotherms, **b** pore size distribution, **c** Raman spectrums and **d** FTIR spectrums of RB, KRB and KRB/MoS_2

Table 1 BET parameters of RB, KRB and KRB/MoS_2

Biochar	S_{BET} ($m^2\ g^{-1}$)	V_{tot} ($cm^3\ g^{-1}$)	V_{mic} ($cm^3\ g^{-1}$)	V_{mic}/V_{tot} (%)	D_p (nm)
RB	8.08	0.02	0.001	5.00	–
KRB	1492.69	1.08	0.40	37.04	2.91
KRB/MoS_2	656.61	0.54	0.11	20.37	3.33

(Fall et al. 2023; Feng et al. 2015). The stretching vibration of the C–O bond caused the characteristic peak at 1100 cm^{-1} (Martínez-Gómez et al. 2023). The characteristic peak shown at 605 cm^{-1} was caused by the stretching of the Mo–S, which further confirmed the successful synthesis of MoS_2 (Fall et al. 2023).

The materials in different stages of preparation were characterized by XPS, as shown in Fig. 3. The full spectrum (Fig. 3a) showed that RB and KRB had C and O elements, while KRB/MoS_2 had C, O, Mo, and S elements. From Table 2, the O/C ratio of RB was 0.36, while the O/C ratio of KRB after modification increased to 0.43, indicating that the etching effect of KOH changed the original structure of the biochar, exposing more oxygen-containing groups. The O/C ratio of KRB/MoS_2 was 0.23, which was due to a series of decomposition reactions and aromatization reactions such as dehydrogenation and decarboxylation of the material during the

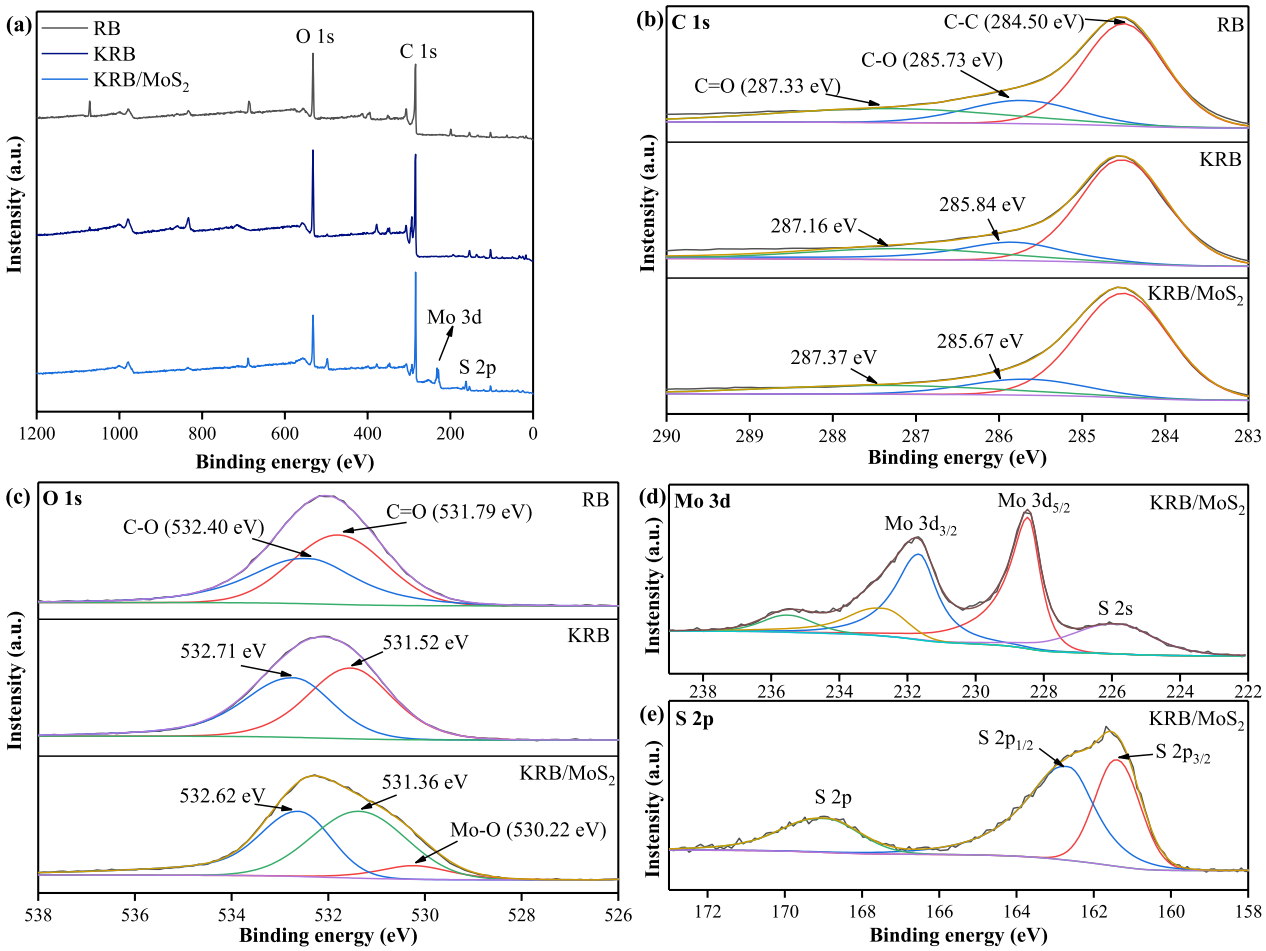

Fig. 3 XPS spectra of **a** survey, **b** C 1s, **c** O 1s, **d** Mo 3d and **e** S 2p of RB, KRB and KRB/MoS_2

Table 2 XPS parameters of RB, KRB and KRB/MoS_2.

	C	O	O/C	Mo	S
RB	73.29	26.71	0.36	–	–
KRB	69.91	30.09	0.43	–	–
KRB/MoS_2	74.17	17.38	0.23	2.96	5.49

high-temperature reaction, which reduced the oxygen-containing groups and thus contributed to the hydrophobic properties of the material.

It could be seen from the C 1s spectrum in Fig. 3b that the proportion of C–C bonds increased continuously after surface modification, while the percentage of C–O increased first and then decreased, which was because the KOH modification exposed the original oxygen-containing group in RB resulting in the increase of the C–O percentage to 22.41%. During the hydrothermal reaction, the oxygen in biochar participated in the reaction and was removed, which eventually reduced the proportion of C–O and increased the proportion of C–C to 70.54%, thus improving the hydrophobic property of KRB/MoS_2. From the O 1s spectrum in Fig. 3c, the change in C–O likewise increased and then decreased with the percentage of C=O decreasing continuously due to the dehydrogenation and decarboxylation of C=O during modification and hydrothermal processes breaking the C=O. In the O 1s spectrum of KRB/MoS_2, a characteristic Mo–O peak of low intensity at 530.22 eV appeared, indicating that a small amount of Mo had formed a chemical bond with O. Figure 3d shows the XPS spectra of Mo 3d. The results showed that there were distinct double peaks at both 231.78 eV and 228.48 eV, which were the characteristic Mo^{4+} $3d_{5/2}$ and Mo^{4+} $3d_{3/2}$ peaks, respectively, confirming the successful loading of MoS_2 (Ahmad et al. 2023). There was a very low intensity peak at the energy level of 235.48 eV, which might be a trace of Mo^{6+} produced during hydrothermal processes

and a lower intensity S 2s peak at 225.88 eV (Liang et al. 2020). The peaks of S $2p_{3/2}$ and S $2p_{1/2}$ appeared at 161.38 eV and 162.78 eV, respectively, in the S 2p spectrum (Fig. 3e) (Lei et al. 2020), which were typical characteristic peaks of S^{2-}, with a weak peak at 169.08 eV indicating the presence of a small amount of higher valence sulfur forms (Wang et al. 2019).

3.2 Contact angle and ice adhesion strength test

To confirm the good hydrophobicity of the coating material, the CA of the substrate and the binder PVDF were tested and the results are shown in Fig. 4a. The CA was minimal for both the uncoated and PVDF coating, measuring just 62.34° and 112.6°, respectively. The CA of RB was 30.03° because there were a large number of oxygen-containing groups in biomass after carbonization, making it more hydrophilic. Whereas, the CA of modified KRB was reduced (CA = 19.46°), which might be due to the water droplets entering the pores after contacting the material. The CA of KRB/MoS_2 coating was 158.32°, and the SA was 4.17°, which was the result of KOH modification and MoS_2 surface modification improving the roughness of the material, and the gradual decrease of the oxygen-containing functional groups such as hydroxyl groups on the surface during high-temperature pyrolysis and hydrothermal processes.

According to Cassie's theory, there was a solid-gas composite interface between water droplets and the coating. Assuming that f_s was the area fraction of the contact interface between water droplets and solids in the composite interface, the CA of the coating satisfied the following Eq. (2) (Bonugli et al. 2012):

$$cos\theta_s = f_1 cos\theta - f_2 \quad (2)$$

where θ is the CA of the surface of KRB/MoS_2 coating, and θs is the CA between the liquid and the glass fiber reinforced plastic substrate.

It could be calculated that the area fraction *fs* of the solid interface on the coating surface was 4.83%, and the rest was air, accounting for 95.17% of the total contact area, which indicated that the actual contact area between water

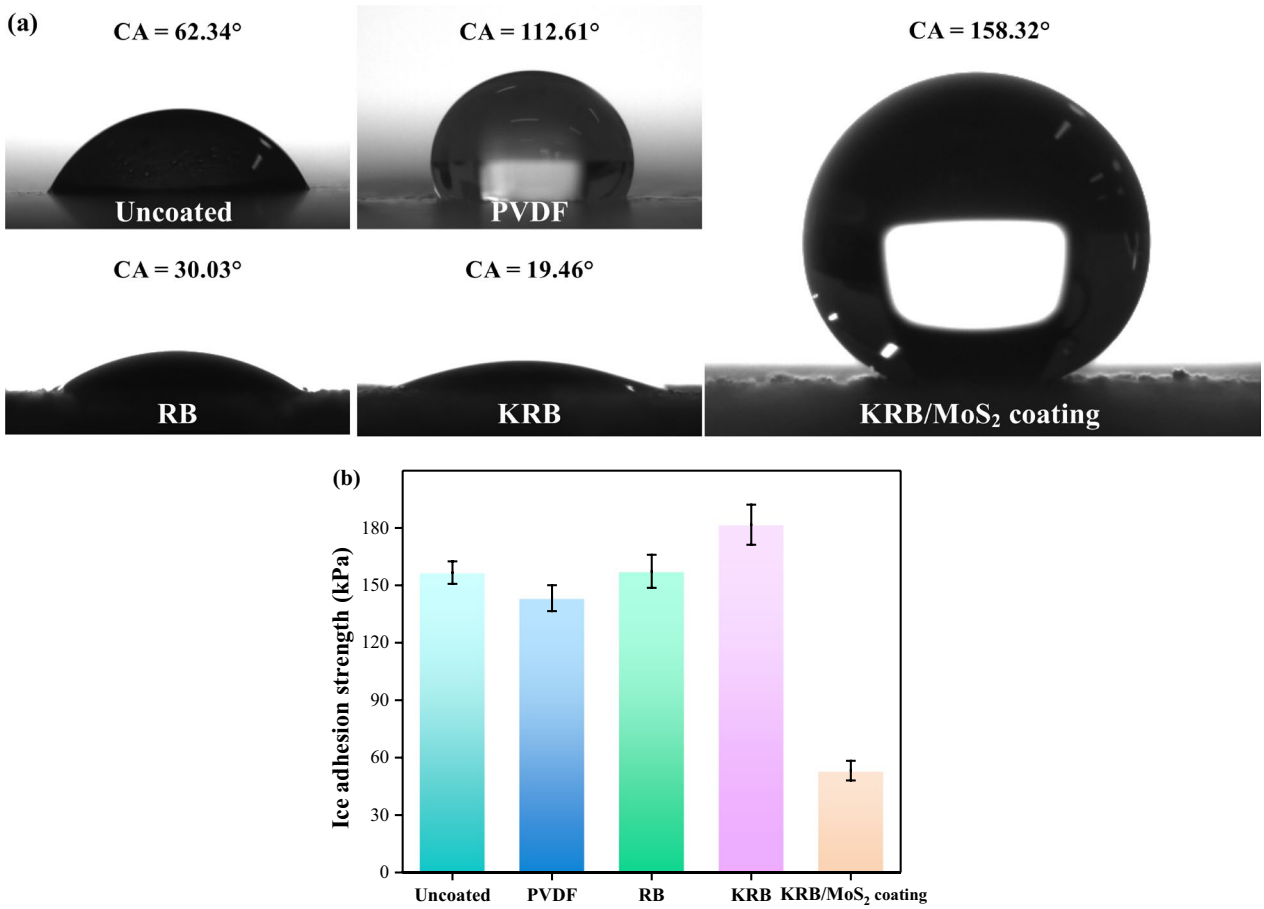

Fig. 4 **a** CA and **b** ice adhesion strength of uncoated, PVDF, RB, KRB and KRB/MoS_2 coating

droplets and the coating surface was low, and the coating could easily make the surface water droplets slide off.

To avoid errors caused by a single measurement, the ice adhesion strength shown in Fig. 4b was the average of the three measurements. It could be seen from the figure that the uncoated substrate had a high adhesion strength of 156.67 kPa, and the PVDF coating had hydrophobic properties, which led to a decrease in adhesion strength to 143.28 kPa. However, RB and KRB contained a large number of hydrophilic groups, and the material pores and ice had a mechanical anchoring effect, which made the adhesion strength stronger. The ice adhesion strength of the KRB/MoS_2 coating was greatly reduced (53.23 kPa), which was 66.02% lower than that of the uncoated. It was because the low surface energy KRB/MoS_2 coating reduced the contact area with water, which made it easier to remove ice.

3.3 Icing wind tunnel experiment

In order to verify the anti-icing performance of the coating under actual conditions, tests were conducted in a wind tunnel simulating a cold environment to investigate the effects of different wind speeds (6, 10 m s^{-1}) and temperatures (− 6, − 8, − 10, − 12, − 14 °C) on the anti-icing effect of the coating. From Fig. 5a, b, it could be seen that blade icing increased gradually with the decrease in temperature at the same wind speed. Moreover, under the same conditions, the icing amount of the KRB/MoS_2 coating was significantly smaller than that of uncoated blades, which proved that the superhydrophobic coating had anti-icing performance.

The variations of blade icing area and icing mass under different conditions are shown in Fig. 5c, d. It could be seen intuitively that the increase in wind speed led to an increase in icing area and mass at the same temperature, and the coating could effectively reduce the icing area and mass in different environments. At a wind speed of 6 m s^{-1}, the icing area and mass could be reduced by 4.48–17.52% and 20.87–43.87%, respectively. At a wind speed of 10 m s^{-1}, the icing area and mass of the coating blade also had a certain protective effect compared with the uncoated blade. When the temperature was − 10 ℃, the icing area and mass decreased by 10.54% and 30.08%, respectively. Figure 5e, f shows the growth of icing area and mass per minute for the uncoated and KRB/MoS_2 coating blades, and it could be seen that the icing area and mass of the uncoated blade grew roughly at a uniform rate. And at 1–3 min, the ice growth of the KRB/MoS_2 coating was smoother, which might be due to the role of the superhydrophobic coating in making the water droplets roll off quickly. At 3–5 min, the ice growth rate of the KRB/MoS_2 coating blade and the uncoated blade was the same, because the coating surface was covered with ice and could not play an anti-icing role.

Figure 6 shows the comparison of uncoated and KRB/MoS_2 coating blades after icing at different temperatures. It was evident that the icing occurred primarily on the leading edge of the blade, and the coated blade exhibited a thinner icing thickness. The presence of spherical water droplets at the trailing end of the leading edge of the KRB/MoS_2 coating blade further substantiated the coating's ability to blow water droplets and even removed them from the blade due to the influence of wind, thereby effectively reducing icing.

3.4 Photothermal performance analysis

The light absorption of biochar material in the wavelength range of 200–2500 nm is shown in Fig. 7a, from which it could be seen that KRB/MoS_2 had a significantly stronger light absorption than RB and KRB. The absorbed sunlight enabled the optical transition of π-bond between the molecules of KRB/MoS_2 material to generate a large amount of heat, thus providing efficient photothermal conversion.

The photothermal properties of the coating were tested at room temperature under one solar intensity irradiation, and the changes in the coating surface temperature during the irradiation are recorded in Fig. 7b. The surface temperature of the uncoated substrate attained equilibrium at 30.9 °C under the light irradiation of 300 s. Because of their light absorption properties, the equilibrium temperatures of RB and KRB were slightly higher than those of uncoated substrates, which were 35.5 ℃ and 41.3 ℃, respectively. The KRB/MoS_2 coating warmed up to 58.3 ℃ after the irradiation of 250 s, which was because the micro-nano structure had good surface roughness, increasing the light illumination area while refracting the light into the material and reducing the reflection, further enhancing the warming rate, indicating that the coating had excellent photothermal conversion performance. The thermal infrared photographs at equilibrium temperature are shown in Fig. 7c.

The thermal stability of the coating was evaluated by cyclic heating and cooling test. The sample was irradiated with a xenon lamp for 7 min, then the xenon lamp was turned off to cool the material surface to room temperature, and the temperature change with time was recorded. From Fig. 7d, it could be seen that the change of the coating surface temperature with time was basically the same during each cycle of the heating and cooling test, indicating that the coating had excellent photo-thermal stability.

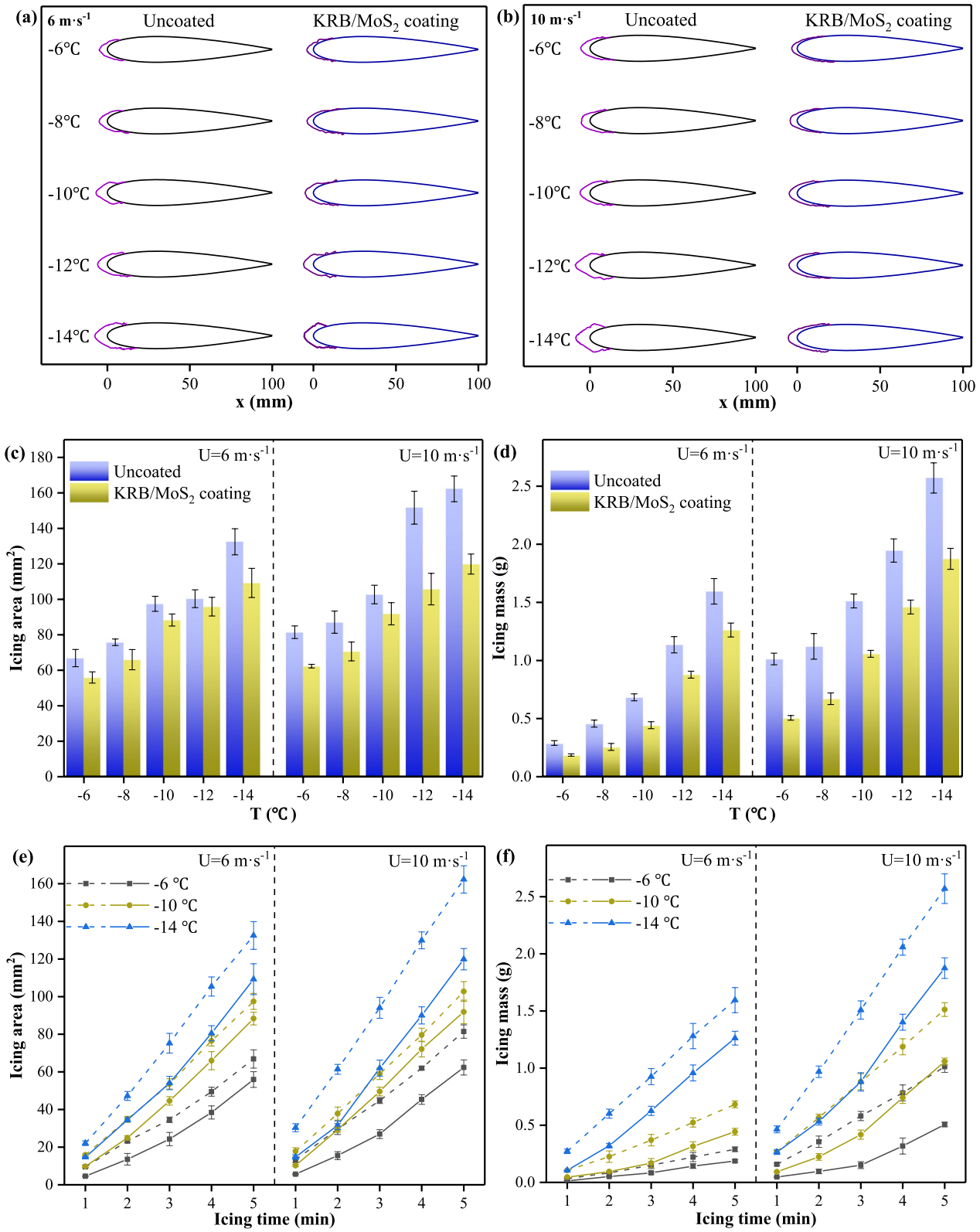

Fig. 5 Blade icing shape at wind speeds of **a** 6 m s^{-1} and **b** 10 m s^{-1}, **c** icing mass and **d** icing area of uncoated and KRB/MoS_2 coating blades, Variation of **e** icing mass and **f** icing area with time (solid line indicates KRB/MoS_2 coating blade, dashed line indicates uncoated blade)

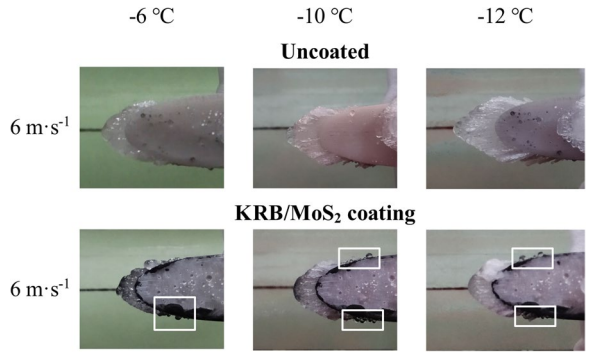

Fig. 6 Blade icing images with wind the speed of 6 m s^{-1} and temperatures of − 6 ℃, − 10 ℃ and − 12 ℃

3.5 Corrosion resistance analysis

Electrochemical impedance testing was an effective way to study the corrosion protection mechanism of materials. The material-electrolyte interface resistance was determined by the size of the radius of the arc in the high-frequency region of the resulting Nyquist diagram. The larger the radius, the greater the resistance, the greater the diffusion path of the electrolyte, and the longer the time required for transfer, which in turn indicated better corrosion protection of the coating.

The Nyquist diagrams of RB, KRB and KRB/MoS_2 coating are shown in Fig. 8. It was clear that RB, KRB and KRB/MoS_2 coating all showed circular arcs in the

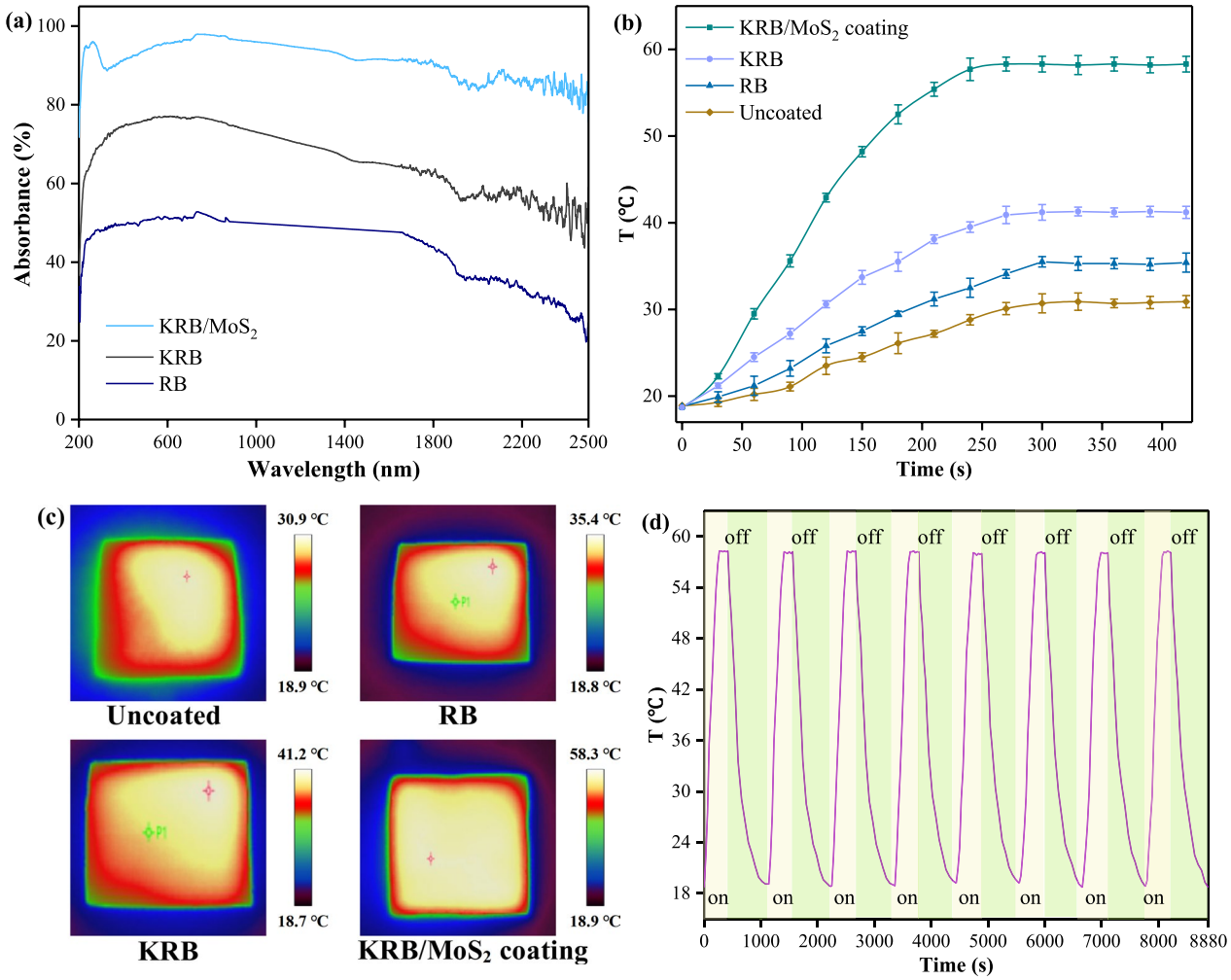

Fig. 7 **a** Absorption curve and reflectance curve, **b** temperature rise and **c** thermal images of uncoated, RB, KRB and KRB/MoS_2 photothermal coating, **d** temperature changes of KRB/MoS_2 photothermal coating at repeated heating-cooling cycles

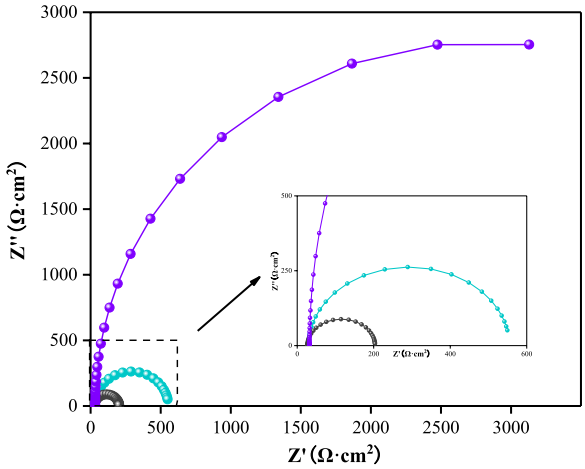

Fig. 8 Nyquist diagram of RB, KRB and KRB/MoS_2 coating in 3.5 wt% NaCl solution

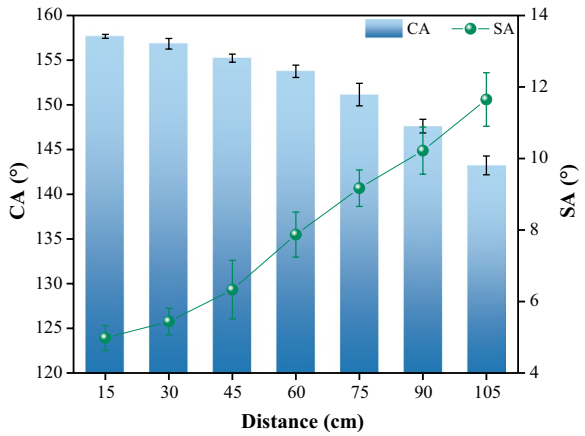

Fig. 9 Mechanical durability of KRB/MoS_2 coating

high-frequency region, indicating that the coating had different degrees of corrosion protection. Among them, the RB coating had the smallest arc radius and the fastest corrosion rate, while the KRB/MoS_2 coating had the largest arc radius and the smallest corrosion rate. This demonstrated that the corrosion resistance of the coating was improved by loading MoS_2, which could be used as a physical barrier to reduce the contact between the corrosive medium and the substrate. The barrier ability of the coating was significantly increased, thus reducing the content of the corrosive medium at the coating-substrate interface.

3.6 Wear resistance test

The wear resistance of the superhydrophobic coating was the main factor affecting its mechanical durability. The variation pattern of CA and SA of the superhydrophobic coating with wear distance is illustrated in Fig. 9. When the wear distance was less than 70 cm, the CA of the coating did not decrease significantly, and the SA increased to a certain extent. When the wear distance reached 75 cm, the CA of the coating was about 147.62°, and the SA was 9.17°, which still maintained a certain hydrophobic property, indicating its excellent mechanical stability. This was due to the firm combination of adhesive and matrix and the stable micro-nano structure of materials.

4 Conclusion

In this study, a superhydrophobic ice-phobic coating was prepared from rice straw biogas residue. High-temperature modification of KOH and hydrothermal loading of MoS_2 gave the material roughness, while dehydrogenation and decarboxylation reactions were generated to enhance the hydrophobic properties of the material. The presence of a large amount of air between the KRB/MoS_2 coating and the water droplets resulted in low icing adhesion strength. The blade icing amount increased as the wind speed increased and the temperature decreased in the wind tunnel test. Under different conditions, the icing area and mass of the ice-phobic coating were smaller, demonstrating good anti-icing performance. KRB/MoS_2 had high-efficiency photothermal conversion ability, which could quickly rise from room temperature to 58.3 ℃ and have photothermal stability. The load of MoS_2 formed a barrier between the substrate and the corrosive medium, which improved the corrosion resistance of the material. This study provided a reference for the recycling of biomass waste and the application of anti-icing on surfaces.

Supplementary Information

The online version contains supplementary material available at https://doi.org/10.1007/s42773-023-00276-0.

Additional file 1: Fig S1. (a) EDS elemental mapping and (b, c) HRTEM images of KRB/MoS_2.

Acknowledgements

The authors are very grateful to the editors and anonymous reviewers for their careful reading, valuable comments and constructive suggestions.

Author contributions

ZL: Methodology, investigation, formal analysis, writing—original draft. YL: Supervision, conceptualization, project administration, methodology, investigation, resources. ZH: Supervision, editing, methodology, validation, writing—original draft. All of the authors participated in the study and agreed to the content of the manuscript. All authors have read and approved the final manuscript.

Funding
This research was funded by the National Natural Science Foundation of China (NSFC) [Grant Number 51976029].

Availability of data and materials
All data generated or analyzed during this study are included in this published article.

Declarations

Competing interests
The authors have no relevant financial or non-financial interests to disclose.

Author details
[1]College of Engineering, Northeast Agricultural University, Harbin 150030, China. [2]School of Materials Science and Engineering, Beijing Institute of Technology, Beijing 100081, China. [3]Heilongjiang Provincial Key Laboratory of Technology and Equipment for Utilization of Agricultural Renewable Resources in Cold Region, Harbin 150030, China.

Received: 1 August 2023 Revised: 30 October 2023 Accepted: 1 November 2023
Published online: 16 November 2023

References

Ahmad MH, Akhond MR, Islam MJ, Rahaman M, Alam RB, Ul-hamid A, Islam MR (2023) A combined experimental and theoretical study on the structural, optical and electronic properties of hetero interface-functionalized MoS2 /Co3O4 nanocomposite. Surf Interfaces 37:102750. https://doi.org/10.1016/j.surfin.2023.102750

Bonugli LO, Puydinger dos Santos MV, de Souza EF, Teschke O (2012) Superhydrophobic polyethylcyanoacrylate coatings. Contact area with water measured by Raman spectral images, contact angle and Cassie–Baxter model. J Colloid Interface Sci 388(1):306–312. https://doi.org/10.1016/j.jcis.2012.08.055

Cheng YH, Wang YR, Zhang X, Zhang JM, He ZY, Wang JJ, Zhang J (2023) Spontaneous, scalable, and self-similar superhydrophobic coatings for all-weather deicing. Nano Res 16(5):7171–7179. https://doi.org/10.1007/s12274-022-5320-4

Fall B, Sall DD, Hémadi M, Diaw AKD, Fall M, Randriamahazaka H, Thomas S (2023) Highly efficient non-enzymatic electrochemical glucose sensor based on carbon nanotubes functionalized by molybdenum disulfide and decorated with nickel nanoparticles (GCE/CNT/MoS2/NiNPs). Sens Actuators Rep 5:100136. https://doi.org/10.1016/j.snr.2022.100136

Feng W, Chen L, Qin M, Zhou XJ, Zhang QQ, Miao YK, Qiu KX, Zhang YZ, He CL (2015) Flower-like PEGylated MoS2 nanoflakes for near-infrared photothermal cancer therapy. Sci Rep 5:13. https://doi.org/10.1038/srep17422

Guan Y, Chen R, Sun G, Liu Q, Liu J, Yu J, Zhu J, Wang J (2023) Ficus religiosa-inspired microstructure-controlled low surface energy coatings with long-term antifouling effect. Colloids Surf Physicochem Eng Aspects 670:131482. https://doi.org/10.1016/j.colsurfa.2023.131482

Guo H, Liu M, Xie C, Zhu Y, Sui X, Wen C, Li Q, Zhao W, Yang J, Zhang L (2020) A sunlight-responsive and robust anti-icing/deicing coating based on the amphiphilic materials. Chem Eng J 402:126161. https://doi.org/10.1016/j.cej.2020.126161

Guo W, Shen H, Li Y, Feng F, Tagawa K (2021) Wind tunnel tests of the rime icing characteristics of a straight-bladed vertical axis wind turbine. Renew Energy 179:116–132. https://doi.org/10.1016/j.renene.2021.07.033

Hou G, Xu L, Taherian H, Jiang W, Song Y (2023) Performance analysis of a hybrid solar-hydrogen-retired EV batteries (REVB) energy system with thermal-electrical loops. Int J Hydrogen Energy. https://doi.org/10.1016/j.ijhydene.2023.03.325

Huang W, Huang J, Guo Z, Liu W (2022) Icephobic/anti-icing properties of superhydrophobic surfaces. Adv Colloid Interface Sci 304:102658. https://doi.org/10.1016/j.cis.2022.102658

Hui B, Chen H, Zhou C, Cai L, Zhang K, Quan F, Yang D (2022) Biochar aerogel-based electrocatalyst towards efficient oxygen evolution in acidic media. Biochar 4(1):39. https://doi.org/10.1007/s42773-022-00163-0

Jlidi Z, Baachaoui S, Raouafi N, Ridene S (2021) Temperature effect on structural, morphological and optical properties of 2D-MoS2 layers: an experimental and theoretical study. Optik 228:166166. https://doi.org/10.1016/j.ijleo.2020.166166

Ju G, Zhou L, Li J, Su C, Zhang L (2023a) Robust metallic-based superhydrophobic composite with rigid micro-skeleton structure for anti-icing/frosting. J Mater Process Technol 316:117916. https://doi.org/10.1016/j.jmatprotec.2023.117916

Ju L, Liu L, Han Y, Yang S, Li G, Lu X, Liu Y, Qiao H (2023b) Robust multi-objective optimal dispatching model for a novel island micro energy grid incorporating biomass waste energy conversion system, desalination and power-to-hydrogen devices. Appl Energy 343:121176. https://doi.org/10.1016/j.apenergy.2023.121176

Karkoosh H, Vithanage M, Sarmah AK (2023) The role of anthocyanin and kaolinite in modifying cabbage leaves biochar for removal of potentially toxic elements and pharmaceutical from aqueous solution. Environ Pollut 325:121435. https://doi.org/10.1016/j.envpol.2023.121435

Ke L, Wu Q, Zhou N, Xiong J, Yang Q, Zhang L, Wang Y, Dai L, Zou R, Liu Y, Ruan R, Wang Y (2022) Lignocellulosic biomass pyrolysis for aromatic hydrocarbons production: pre and in-process enhancement methods. Renew Sust Energ Rev 165:112607. https://doi.org/10.1016/j.rser.2022.112607

Kumar A, Bhattacharya T, Shaikh WA, Roy A, Chakraborty S, Vithanage M, Biswas JK (2023) Multifaceted applications of biochar in environmental management: a bibliometric profile. Biochar 5(1):11. https://doi.org/10.1007/s42773-023-00207-z

Lei L, Huang DL, Lai C, Zhang C, Deng R, Chen YS, Chen S, Wang WJ (2020) Interface modulation of Mo2C@foam nickel via MoS2 quantum dots for the electrochemical oxygen evolution reaction. J Mater Chem A 8(30):15074–15085. https://doi.org/10.1039/d0ta05045h

Li Y, Yang S, Feng F, Tagawa K (2023) A review on numerical simulation based on CFD technology of aerodynamic characteristics of straight-bladed vertical axis wind turbines. Energy Rep 9:4360–4379. https://doi.org/10.1016/j.egyr.2023.03.082

Liang Z, Xue Y, Guo Y, Zhang G, Cui H, Tian J (2020) Rationalizing and controlling the phase transformation of semi-metallic 1T′-phase and semiconductive 2H-phase MoS2 as cocatalysts for photocatalytic hydrogen evolution. Chem Eng J 396:125344. https://doi.org/10.1016/j.cej.2020.125344

Liu Z, Sun Y, Xu X, Meng X, Qu J, Wang Z, Liu C, Qu B (2020) Preparation, characterization and application of activated carbon from corn cob by KOH activation for removal of hg(II) from aqueous solution. Bioresour Technol 306:123154. https://doi.org/10.1016/j.biortech.2020.123154

Liu J, Dong Y, Zhang L, Liu W, Zhang C, Shi Y, Lin H (2021) Regulating superoxide radicals and light absorption ability for enhancing photocatalytic performance of MoS2@Z by CeO2 rich in adsorbed oxygen. J Clean Prod 322:129059. https://doi.org/10.1016/j.jclepro.2021.129059

Liu Z, Zhen F, Zhang Q, Qian X, Li W, Sun Y, Zhang L, Qu B (2022) Nanoporous biochar with high specific surface area based on rice straw digestion residue for efficient adsorption of mercury ion from water. Bioresour Technol 359:127471. https://doi.org/10.1016/j.biortech.2022.127471

Liu Y, Guo R, Liu J, Zhang Q (2023a) Robust PFMA/CNTs composite PDMS superhydrophobic film via SI-CuCRP method for efficient anti-icing. Colloids Surf Physicochem Eng Aspects 660:130913. https://doi.org/10.1016/j.colsurfa.2022.130913

Liu Z, Feng F, Li Y, Sun Y, Tagawa K (2023b) A corncob biochar-based superhydrophobic photothermal coating with micro-nano-porous rough-structure for ice-phobic properties. Surf Coat Technol 457:129299. https://doi.org/10.1016/j.surfcoat.2023.129299

Liu Z, Li Y, Sun Y, Feng F, Tagawa K (2023c) Preparation of biochar-based photothermal superhydrophobic coating based on corn straw biogas residue and blade anti-icing performance by wind tunnel test. Renew Energy 210:618–626. https://doi.org/10.1016/j.renene.2023.04.098

Martínez-Gómez Á, Andrés MF, Barón-Sola Á, Díaz-Manzano FE, Yousef I, Mena IF, Díaz E, Gómez-Torres Ó, González-Coloma A, Hernández LE, Escobar C (2023) Biochar from grape pomace, a waste of vitivinicultural origin, is effective for root-knot nematode control. Biochar 5(1):30. https://doi.org/10.1007/s42773-023-00228-8

Miao F, Luo Z, Zhou Q, Du L, Zhu W, Wang K, Zhou J (2023) Study on the reaction mechanism of C8+ aliphatic hydrocarbons obtained directly from biomass by hydropyrolysis vapor upgrading. Chem Eng J 464:142639. https://doi.org/10.1016/j.cej.2023.142639

Molnár G, Ürge-Vorsatz D, Chatterjee S (2022) Estimating the global technical potential of building-integrated solar energy production using a high-resolution geospatial model. J Clean Prod 375:134133. https://doi.org/10.1016/j.jclepro.2022.134133
Mu Z, Guo W, Li Y, Tagawa K (2023) Wind tunnel test of ice accretion on blade airfoil for wind turbine under offshore atmospheric condition. Renew Energy 209:42–52. https://doi.org/10.1016/j.renene.2023.03.126
Qi H, Lei X, Gu J, Zhang Y, Gu X, Zhao G, Yu J (2023) Low modulus of polydimethylsiloxane organogel coatings induced low ice adhesion. Prog Org Coat 177:107435. https://doi.org/10.1016/j.porgcoat.2023.107435
Shamshiri M, Jafari R, Momen G (2023) A novel hybrid anti-icing surface combining an aqueous self-lubricating coating and phase-change materials. Prog Org Coat 177:107414. https://doi.org/10.1016/j.porgcoat.2023.107414
Tong G, Li Y, Tagawa K, Feng F (2023) Effects of blade airfoil chord length and rotor diameter on aerodynamic performance of straight-bladed vertical axis wind turbines by numerical simulation. Energy 265:126325. https://doi.org/10.1016/j.energy.2022.126325
Wang Y, Wei R, Zhang B, Lv H, Xu DD, Hao QL, Liu B (2019) Template-assisted self-sulfuration formation of MoS2 nanosheets embedded in ordered mesoporous carbon for lithium storage. ACS Appl Energ Mater 2(9):6158–6162. https://doi.org/10.1021/acsaem.9b01262
Wang D, Fu Q, Tian J, Zhou H, Liu R, Zhan D, Peng Z, Han C (2023a) Piezoelectric polarization induced by dual piezoelectric materials ZnO nanosheets/MoS2 heterostructure for enhancing photoelectrochemical water splitting. J Colloid Interface Sci. https://doi.org/10.1016/j.jcis.2023.09.157
Wang L, Wang T, Hao R, Wang Y (2023b) Synthesis and applications of biomass-derived porous carbon materials in energy utilization and environmental remediation. Chemosphere 339:139635. https://doi.org/10.1016/j.chemosphere.2023.139635
Wang Z, Xu Y, Yang T, Liu Y, Zheng T, Zheng C (2023c) Effects of biochar carried microbial agent on compost quality, greenhouse gas emission and bacterial community during sheep manure composting. Biochar 5(1):3. https://doi.org/10.1007/s42773-022-00202-w
Wu B, Cui X, Jiang H, Wu N, Peng C, Hu Z, Liang X, Yan Y, Huang J, Li D (2021) A superhydrophobic coating harvesting mechanical robustness, passive anti-icing and active de-icing performances. J Colloid Interface Sci 590:301–310. https://doi.org/10.1016/j.jcis.2021.01.054
Wu SW, Liang ZY, Li YP, Chay S, He ZY, Tan SC, Wang JJ, Zhu XY, He XM (2022) Transparent, photothermal, and icephobic surfaces via layer-by-layer assembly. Adv Sci 9(14):7. https://doi.org/10.1002/advs.202105986
Xiang T, Chen X, Lv Z, Tong W, Cao J, Shen Y, Liao B, Xie Y, Zhang S (2023) Stable photothermal solid slippery surface with enhanced anti-icing and de-icing properties. Appl Surf Sci 624:157178. https://doi.org/10.1016/j.apsusc.2023.157178
Xu X, Sun Y, Sun Y, Li Y (2022) Bioaugmentation improves batch psychrophilic anaerobic co-digestion of cattle manure and corn straw. Bioresour Technol 343:126118. https://doi.org/10.1016/j.biortech.2021.126118
Xu X, Yan M, Sun Y, Li Y (2023) Bioaugmentation with cold-tolerant methanogenic culture to boost methane production from anaerobic co-digestion of cattle manure and corn straw at 20℃. Chem Eng J 466:143183. https://doi.org/10.1016/j.cej.2023.143183
Xue YQ, Wang YB, Wang YH, Liang WY, Wang FX, Zhu DY, Zhao HY (2023a) Functionalized superhydrophobic MWCNT/PEI nanocomposite film with anti-icing and photo-/electrothermal deicing properties. Mater Chem Phys 297:12. https://doi.org/10.1016/j.matchemphys.2023.127385
Xue YQ, Wang YB, Wang YH, Liang WY, Wang FX, Zhu DY, Zhao HY (2023b) Functionalized superhydrophobic MWCNT/PEI nanocomposite film with anti-icing and photo-/electrothermal deicing properties. Mater Chem Phys 297:127385. https://doi.org/10.1016/j.matchemphys.2023.127385
Yang K, Liu Q, Lin Z, Liang Y, Liu C (2022) Investigations of interfacial heat transfer and phase change on bioinspired superhydrophobic surface for anti-icing/de-icing. Int Commun Heat Mass Transf 134:105994. https://doi.org/10.1016/j.icheatmasstransfer.2022.105994
Yoon K, Cho D-W, Tsang DCW, Bolan N, Rinklebe J, Song H (2017) Fabrication of engineered biochar from paper mill sludge and its application into removal of arsenic and cadmium in acidic water. Bioresour Technol 246:69–75. https://doi.org/10.1016/j.biortech.2017.07.020
Yue Z, Wang Y, Lan Z, Hu K, Shi S, Zhang J, Meng Q, Nie Y, Sun Q, Shen X (2023) Bilayer bamboo for photothermal trap and large-scale anti-icing. Ind Crop Prod 194:116290. https://doi.org/10.1016/j.indcrop.2023.116290
Zhang L, Gao C, Zhong L, Zhu L, Chen H, Hou Y, Zheng Y (2022) Robust photothermal superhydrophobic coatings with dual-size micro/nano structure enhance anti-/de-icing and chemical resistance properties. Chem Eng J 446:137461. https://doi.org/10.1016/j.cej.2022.137461
Zhang J, Shao J, Zhang X, Rao G, Krivoshapkin P, Krivoshapkina E, Yang H, Zhang S, Chen H (2023a) Broccoli-shaped Cu-BTC/biochar composite with enhanced water stability for toluene adsorption: influence of humid air aging. Fuel 335:127013. https://doi.org/10.1016/j.fuel.2022.127013
Zhang Y, Guo W, Li Y, Chi H, Zhao P, Tagawa K (2023b) An experimental study of icing distribution on a symmetrical airfoil for wind turbine blade in the offshore environmental condition. Ocean Eng 273:113960. https://doi.org/10.1016/j.oceaneng.2023.113960
Zheng J, Liu R, Liu D, Weng Z, Song G, Li W, Wang Z (2023) Slippery liquid infused porous surfaces with anti-icing performance fabricated by direct laser interference lithography. Prog Org Coat 175:107308. https://doi.org/10.1016/j.porgcoat.2022.107308